Interfacial Convection during Evaporation of Binary Mixtures from Porous Obstacles

S. Post, I. Urukova, and E. Tsotsas
Thermal Process Engineering, Otto-von-Guericke-University, Universitätsplatz 2, D-39106 Magdeburg, Germany

DOI 10.1002/aic.10557

A novel experimental approach is proposed to investigate the influence of interfacial convection on liquid-side mass transfer. Specifically, a binary liquid mixture (water and isopropanol) is evaporated from a porous obstacle into inert gas (air). The change of liquid bulk molar fraction with changing amount of liquid (concentration curve) is observed. The porous obstacle is a plate with parallel planar gaps, or a packed bed of spherical particles, both completely filled with the liquid. Without interfacial convection, that is, for the undisturbed state of the system, the liquid is quiescent and evaporation should be nonselective. Consequently, measured selectivities not only prove the existence of interfacial convection, but also give the opportunity of evaluating liquid-side mass transfer coefficients and enhancement factors for the disturbed state of the system. This evaluation is conducted with the help of a one-dimensional model for mass and heat transfer. If applied to the undisturbed state of the system, the same model provides driving density and molar fraction differences in the form of Rayleigh and Marangoni numbers. It is shown that the extent of interfacial convection can be controlled by operating parameters such as the gas bulk temperature, whereas it also depends on structural parameters such as gap width or particle diameter. Thermally driven and molar fraction driven Rayleigh and Marangoni convection may coexist. With the described method much higher enhancement factors than ever previously reported could be detected. The dependency of such enhancement factors on the Rayleigh or Marangoni number is considerably stronger than reported in the literature. Some aspects concerning the consideration of liquid-side heat transfer or permeability and structure of the medium are discussed, and nonselective experiments corresponding to stable configurations are identified. First attempts toward correlation of the results are outlined, along with the potential of the method for future research. © 2005 American Institute of Chemical Engineers *AIChE J,* 51: 3257–3274, 2005

Keywords: interfacial convection, enhancement of mass transfer, planar gaps, packed beds, evaporation, binary liquid mixture, selectivity

Introduction

Gradients of temperature or molar fraction (more general: electrochemical potential) along the boundary of a liquid phase, or between this boundary and the bulk, can give rise to spontaneous flow, which is called interfacial convection or interfacial turbulence. This presupposes that either density or interface tension gradients result from the gradients of the state variables, so that we usually distinguish between Rayleigh and Marangoni convection, respectively. Marangoni convection may be driven by temperature differences (thermocapillarity) or by molar fraction differences, and the same is true for Rayleigh convection.

Stability analysis is one important instrument for the study of such phenomena. Since the derivation by Lord Rayleigh, which refers to a liquid layer with temperature-dependent density

---

Present addresses: S. Post, BASF Aktiengesellschaft, GIC/P–Q920, 67056 Ludwigshafen, Germany (stephan.post@basf-ag.de); I. Urukova, Applied Thermodynamics, University of Kaiserslautern, Erwin-Schrödinger-Straβe, D-67663 Kaiserslautern, Germany (urukova@mv.uni-kl.de).

Correspondence concerning this article should be addressed to E. Tsotsas at evangelos.tsotsas@vst.uni-magdeburg.de.

heated from below and cooled at the boundary to a gas phase, a vast amount of literature has appeared in this field. Recent publications expand the classical analysis by considering such phenomena as waves of the deformable interface[1] or the temperature dependency of physical properties other than density.[2] Combined, thermally driven Rayleigh and Marangoni convection is treated by Bragard and Velarde[3] with respect to the form of the resulting cells, and Birikh et al.[4] investigate boundary conditions different from those in the original formulation of the problem. Thermally driven Marangoni convection is discussed with respect to modulation by weak nonplanar shear by Or and Kelly,[5] spatially limited gas phase and pattern formation by Golovin et al.,[6] and deep liquid layers by Hashim and Wilson.[7] Boeck and Thess[8] apply direct numerical simulation to study pattern formation, whereas Li et al.[9] investigate bridges, consisting of a cylindrical liquid phase surrounded by a thin annulus of a second liquid. Approximate solutions for deep liquids with various boundary conditions are provided by Tan and Thorpe.[10] Marangoni convection driven by molar fraction gradients and reversible surface reaction is analyzed by von Gottberg et al.[11] and Mendes-Tatsis and Pérez de Ortiz.[12] Kang et al.[13] apply the propagation theory to analyze numerically the stability during desorption at the interface without gas-side mass transfer resistance, whereas Skarda and McCaughan[14] approach analytically molar fraction or thermally driven Marangoni convection in multicomponent mixtures. Control concepts with feedback strategies are discussed by Bau.[15]

Stability analysis for liquid–liquid systems has been initiated by the work of Sternling and Scriven,[16] and developed further by many investigators, including Pérez de Ortiz and Sawistowski,[17] Imaishi and Fujinawa,[18] Reichenbach and Linde,[19] and Wassmuth et al.[20] Parallel to this has been the development and application of experimental techniques for the visualization and measurement of velocity and concentration fields (various optical, Schlieren, and laser methods, holographic interferometry; see the recapitulation by Wolf[21] and the recent reports by Chai and Zhang[22] and Guzun-Stoica et al.[23]).

However, stability analysis and visualization only partially answer the question, how driving potentials for interface convection emerge during technical processes with mass and heat transfer such as extraction, absorption, or distillation, and they do not answer the still more important question about the enhancement of such processes by the resulting interface convection. Experimental work coupled with empirical correlations and simplified models is necessary to this purpose. Such work referring to liquid–liquid extraction has been recapitulated by Pertler et al.[24] and Wolf,[21] and will not be discussed in more detail here. It should just be noticed that planar liquid layers, quiescent or mechanically agitated emulsions, stratified channel flows, falling films, and irrigated packed beds have been investigated, with a clear trend to single-drop experiments that promise a more fundamental observation and understanding of the relevant transport phenomena (see, for example, Henschke and Pfennig[25]).

As to liquid–gas or liquid–vapor systems, the augmentation of mass transfer by interfacial convection has been discussed by Semkov and Kolev,[26] Proctor et al.,[27] and Wu et al.,[28] who also summarize the results of older experimental investigations on absorption or distillation conducted mainly in packed-bed columns. Such work reveals, on the one hand, considerable increases of separation efficiency that can be attributed to interfacial phenomena, but also clearly shows the difficulties related with an accurate evaluation of column experiments arising from the influence of axial dispersion, liquid distribution, wettability, and droplet formation. To avoid these difficulties several authors[29-31] followed the so-called spreading method introduced by Ruckenstein and coworkers[32] for the experimental investigation of the impact of interfacial convection on liquid-side mass transfer during absorption. In the spreading method, a solute with low surface tension is injected from a capillary tube on the liquid–gas interface, flows as a thin film in radial direction, induces Marangoni convection, and enhances the rate of absorption of the gas in the liquid. A theoretical treatment is possible, however, only after a number of simplifying assumptions for the system that is complex (three components in the liquid in the vicinity of the interface) and, in fact, dissimilar to the case of driving potentials evolving during mass transfer operations.

Along with a number of correlations, several more or less simple models based on surface renewal, penetration, or cell rotation concepts have been proposed in the literature by, among others, Ruckenstein and Berbente,[33] Linde and Schwarz,[34] Ostrovskii et al.,[35] Imaishi et al.,[36] and Pikkov and Rabinovich.[37] In these correlations and models the dependency of enhancement factors on the Marangoni (or Rayleigh) number is described with exponents ranging between 0.25 and 0.67, with the majority opting for an exponent near 0.5. Enhancement factors have values of up to 5, usually lower. Still more unclear is the influence of the Schmidt number. In a recent publication Sun et al.[38] point out the fortuity of knowledge about how Rayleigh and Marangoni convection combine with each other, and approach this topic on the basis of experiments with absorption or desorption of a gas to/from a liquid film.

Addressing the evident need for further data on the influence of interfacial convection on mass transfer, a novel experimental method that can be used to this purpose will be presented. The method is based on the evaporation of a binary liquid mixture into inert gas, a process that has been thoroughly discussed by many authors, especially by Schlünder and coworkers.[39] The goal of such investigations has been to find out how the selectivity of the evaporation depends on mass transfer. As we will see later on, the analysis predicts vanishing selectivities in the case of control by liquid-side mass transfer. However, attempts to realize experimentally this limiting case by artificially inhibiting the liquid-side mass transfer with the help of a porous obstacle have rarely been successful, which was attributed to interface convection.[40] In the present investigation, the objective of previous work is inverted: that is, from understanding the influence of mass transfer on selectivity to deriving from measured selectivities conclusions about the influence of interfacial convection on the liquid-side mass transfer.

Specifically, the purpose of the present paper is to:

- Present experimental apparatuses designed to enable the determination of residual concentration curves during the batch

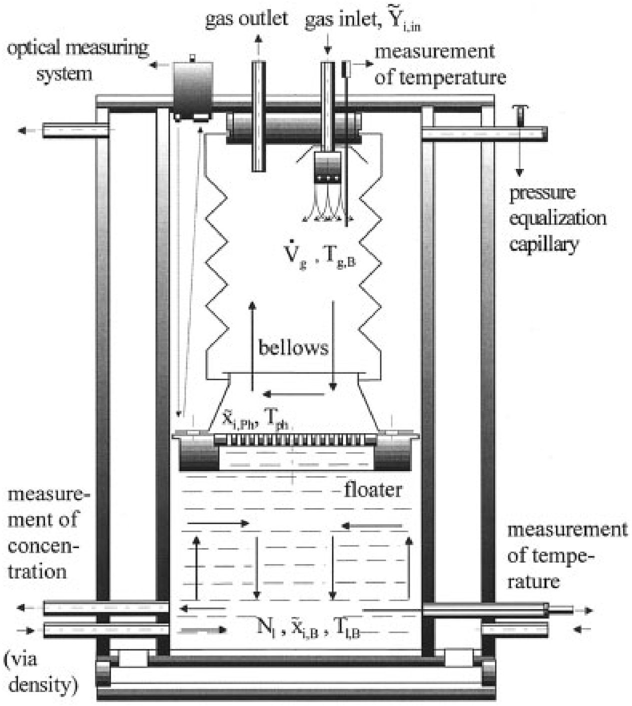

Figure 1. Apparatus for the investigation of the evaporation of a binary mixture from planar gaps into inert gas.

evaporation of a binary liquid mixture from a porous obstacle to inert gas in a reliable and reproducible way under well-defined conditions.

- Discuss experimental results and show that measured concentration curves and selectivities clearly prove the existence and indicate the intensity of interfacial convection. Show that the intensity of interfacial convection can be deliberately controlled by changing the bulk temperature of the gas phase, and discuss the influence of further operating parameters.
- Present a simplified, one-dimensional model for the mass and heat transfer and show, how liquid-side mass transfer coefficients can be derived with its help from the measured concentration curves. Such coefficients express the influence of interfacial convection on liquid-side mass transfer and can be transformed to enhancement factors (*Eh*).
- Show that the same model can be applied to the limiting case without interfacial convection (undisturbed state) to derive relevant driving forces (density and surface tension differences) in the form of Rayleigh (Ra) and Marangoni (Ma) numbers.
- Discuss the phenomenology of the experimental data, after their translation in *Eh*, Ra, and Ma. Show that four different types of interfacial convection (Rayleigh convection driven by temperature or molar fraction gradients, Marangoni convection driven by temperature or molar fraction gradients) can be responsible for the overall effects, in various combinations.

Slabs with a number of parallel planar gaps and packed beds will be the porous obstacles corresponding to research work by Post[41] and Urukova.[42] In both cases, the liquid system considered will be isopropanol and water, and the inert gas will be air.

The discussion of the above-mentioned aspects will reveal values of the enhancement factor in a range that has never been investigated before, and lead to scarcely treated topics, such as interfacial convection in porous media by a combination of temperature and molar fraction profiles.[43] Although the present, experimentally oriented work will, at best, only touch such topics, we do hope that it might provide some additional momentum and data for a complex and interesting field of engineering research. Although first correlation attempts will be outlined, they are only preliminary and not the focus of this investigation. Completely outside of our present scope are flow visualization, stability analysis, and two-dimensional modeling of the transport phenomena in the porous obstacle. The same holds for the possible extrapolation of the results to situations without porous obstacle, such as those appearing in distillation or absorption columns.

Experimental Apparatuses and Procedures

The experimental apparatus for evaporation from planar gaps[41] is depicted schematically in Figure 1. Its construction fulfills the following requirements:

- Evaporation can take place only from the porous obstacle that separates the liquid from the gas phase. To this purpose the sliced, rectangular slab that constitutes the obstacle (Figure 2) is inserted in a rectangular floater frame.
- The floater is free to move within certain limits. Because of this movability and initial fine adjustment with the help of small weights, the planar gaps are completely filled with liquid at any time, that is, the upper edge of the floater is identical with the liquid surface. Consequently, the amount of liquid still present after a certain evaporation time (N_l) can be calculated from the position of the floater. The latter is measured with the help of a laser sensor.
- In spite of the freedom of movement of the floater, evaporation cannot occur through the gap between floater and the cage of the device. Such bypass evaporation is suppressed by a flexible and air-tight bellows that separates the gas space above the floater from the residual gas space of the apparatus. The amount of vapor necessary to saturate the latter is negligible.
- The temperature in the bulk of the gas phase above the porous obstacle ($T_{g,B}$) is measured by a temperature sensor and regulated to a prescribed, constant value by an external thermostat. Relatively large volume rates ($\dot{V}_g$) of dried air ($\tilde{Y}_{i,in} = 0$) inserted in the apparatus by a distributor system create well-mixed conditions in the gas bulk. Furthermore, they give

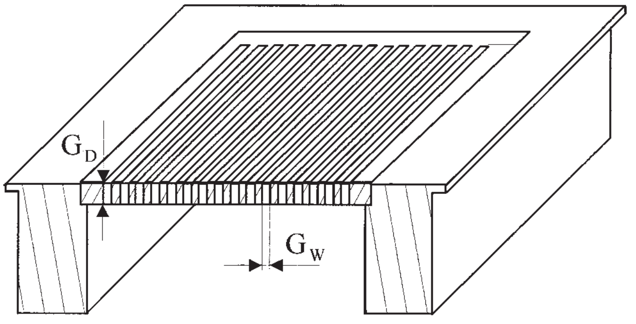

Figure 2. Cross-sectional view of the floater with insert, geometrical parameters of the gaps.

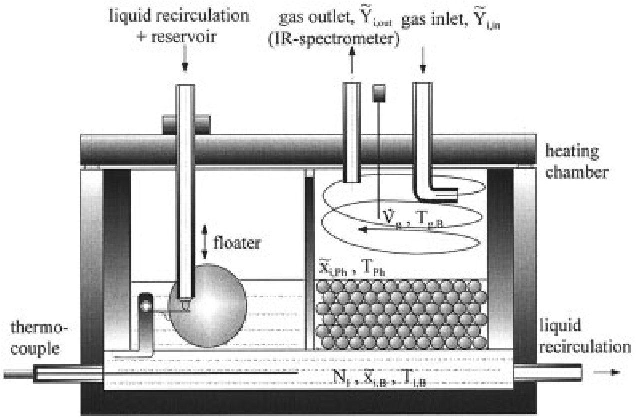

Figure 3. Apparatus for the investigation of the evaporation of a binary mixture from packed beds into inert gas.

rise to relatively large gas-side mass transfer coefficients and, in combination with low evaporation temperatures, keep the vapors dilute in the gas phase.

- A pump recirculates in closed, tempered loop a certain amount of the liquid. As a result of this recirculation, the molar fraction is spatially uniform in the bulk of the liquid. The respective value, $\tilde{x}_{1,B}$, is derived from density measurements conducted in the recirculation loop by means of a highly sensitive U-tube oscillatory device.
- In spite of the mixing action of the recirculation in respect to the bulk of the liquid phase, no forced convective mixing takes place in the planar gaps of the floater insert. This has been checked by variation of the recirculation rate, fluid-dynamic calculations, and tracer (color, salt) tests.
- By temperature control of the recirculation circuit and of the liquid-filled coat of the apparatus, the temperature in the bulk of the liquid phase ($T_{l,B}$) can be kept to a prescribed, constant and spatially uniform value. This value may be different from the temperature in the bulk of the gas phase.

The device for evaporation from a packed bed of particles[42] is depicted schematically in Figure 3. It also fulfills all the discussed requirements. Major differences to the arrangement according to Figure 1 are that:

- The temperature in the bulk of the liquid phase ($T_{l,B}$) is set to a prescribed value by putting the entire evaporation cell in a heating chamber.
- An external reservoir and a floater are used to constantly keep the level of the liquid at the upper edge of the porous obstacle.
- The amount of liquid still present after a certain evaporation time (N_l) and the molar fraction in the bulk of the liquid phase ($\tilde{x}_{1,B}$) are calculated with the help of mass balances from the molar fractions of the evaporating components in the outlet gas measured by means of infrared spectroscopy. Precise calibration and consideration of cross-sensitivity provide an excellent accuracy of the IR readings.

As to the constructive details, the evaporation cell consists of a cylindrical, stainless steel tube (inner diameter: 60 mm), which is—with the exception of the connections for gas and liquid—hermetically closed. A second block of stainless steel is placed into this tube. In this block, which is shorter than the outer tube, two cylindrical holes of equal diameters have been machined. In this way, both the bulk of the liquid phase and the space to be filled with the packed bed are properly defined. The bed is supported by a thin-wire sieve, with apertures somewhat smaller than the particle diameter. Advantages of the experimental design after Figure 3 are seen in the fact that the porous obstacle is not moving, the liquid level is easier to adjust, and the temperature control of the liquid phase is more efficient.

The desired output of the experiment is, in both cases, the function $N_l/N_{l,0}(\tilde{x}_{1,B})$ that describes the change of liquid bulk molar fraction with decreasing amount of liquid, with reference of the latter to the initial amount ($N_{l,0}$). This function is denoted in the following as the *concentration curve*. Measurement of the concentration curve up to very low values of $N_l/N_{l,0}$ with the device of Figure 1 would require a large translatorial movement of the floater in the vertical direction and a dilatability, which the used bellows cannot provide. Consequently, the measurement of the entire concentration curve is not possible in one pass. Instead, the run has to be interrupted and the device is filled with an additional amount of liquid (ΔN_l) that has the same molar fraction ($\tilde{x}_{1,B}$) as the residual amount of liquid at the specific time. After *n* repetitions of the procedure the ordinate of the concentration curve is

$$\frac{N_l}{N_{l,0}} = \frac{N_{l,1}}{N_{l,0}} \frac{N_{l,2}}{(N_{l,1} + \Delta N_l)} \cdots \frac{N_{l,n+1}}{(N_{l,n} + \Delta N_l)} \tag{1}$$

In the device of Figure 3 liquid is added in the external reservoir. The molar fraction of residual liquid was determined off-line before every refilling of the reservoir by means of a very accurate U-tube oscillatory densitometer. The resulting values of $\tilde{x}_{1,B}$ have always been in excellent agreement with the values derived from the IR readings and the mass balances. As a consequence of this way of measurement and of the very moderate temperatures, the time necessary to determine one complete concentration curve is long, up to one week. The addition of liquid is conducted, depending on the specific operating conditions, two or three times a day.

Although the long duration of one run is the price to be paid for the segmentation of the experiment and for the moderate temperature level, the latter has—in combination with the relatively high gas flow rates used—one major advantage: that is, high dilution of the vapors in the gas phase, so that isopropanol and water diffuse simultaneously through the air in the same way as the respective pure components would have done. Consequently, it is not necessary to use the Stefan–Maxwell equations for the gas phase, which facilitates the subsequent evaluation. More important, the gas-side mass transfer coefficients of isopropanol and water can be determined by separate evaporation experiments with the pure components, so that the subsequent evaluation can concentrate on the liquid-side mass transfer without any reconsideration or adjustment of gas-side transport phenomena. The details and results of the derivation of gas-side mass transfer coefficients and the Lewis exponent (Eq. 14) from pure-liquid evaporation experiments are discussed by Post[41] and Urukova,[42] and will not be repeated here.

With reference to the same PhD theses, we also refrain from repeating the correlations used for the determination of the various relevant properties of the pure components and the mixture, including binary diffusion coefficient, thermal conductivity, density, and surface tension of the liquid phase in dependency of molar fraction and temperature. Good knowledge of the material properties has been one reason for the choice of isopropanol (index: $i = 1$) and water (index: $i = 2$) as the liquid system for the present investigation. The differences in density and surface tension of the pure components, as a presupposition for the investigation of respective instabilities are the second reason. Remember that isopropanol has both lower density and surface tension ($\rho_{l,1} = 781.3$ kg/m^3, $\sigma_{l,1} = 0.02333$ N/m at 25°C) compared to those of water ($\rho_{l,2} = 997.0$ kg/m^3, $\sigma_{l,2} = 0.07540$ N/m at 25°C), and that both the density and the surface tension decrease with increasing temperature over the entire molar fraction range.

As to the porous obstacles, the sliced slabs according to Figure 2 consisted of a specialty polyurethane polymer (Prolab 50®, Axson Ltd.) with nonporous and homogeneous structure, low density, and very low thermal conductivity. The parallel, planar gaps have been cut out very accurately by means of a laser manufacturing technique. Slabs of different gap widths ($G_W = 0.5$, 1.0, and 1.5 mm) and different gap depths ($G_D = 1.0$, 2.0, 4.0, and 8.0 mm) have been used. The length of the gaps varied between 16 and 70 mm. Because this dimension has not been found to be of significance, it will not be stated in the subsequent presentation of experimental results. The number of the gaps varied between 24 and 144 and is also without significance for the results. However, a sufficient number of parallel gaps is necessary to keep the time necessary to complete one experiment within tolerable limits. The investigated packed beds were made of polished glass spheres. Five closely monodispersed fractions with average particle diameters of $d_p = 0.23$, 0.57, 1.30, 2.60, and 3.50 mm have been used. The bed height h varied in value from 5 to 25 mm, with bed porosities ψ ranging in value from 0.35 to 0.38. The permeability of the beds, defined by

$$\kappa = \frac{1}{150} \frac{d_p^2 \psi^3}{(1 - \psi)^2} \tag{2}$$

ranged in value from $\kappa = 4.02 \times 10^{-11}$ to $\kappa = 9.30 \times 10^{-9}$ m^2. The particle density was determined as $\rho_p = 2470$ kg/m^3 and the particle thermal conductivity was, according to the producer, $\lambda_p = 0.8$ W m^{-1} K^{-1}.

Without spontaneous convection, the evaporating components must overcome the entire porous obstacle by molecular diffusion before reaching the interface. The gaps or beds may thus be considered as the analogon of a very thick laminar boundary layer according to film theory. This provides a clear reference value for the liquid-side mass transfer coefficient, with consequences that will be discussed in the next section.

Prediction of the limiting case without a porous obstacle (see next section) provides an overall validation of the experimental technique. The reproducibility of measured concentration curves was excellent.

Experimental Results for Evaporation from Planar Gaps and Their Interpretation in Terms of Interfacial Convection

In a total of 29 experiments conducted with sliced slabs as the porous obstacle, the liquid bulk temperature and the gas flow rate were kept constant at $T_{l,B} = 298.15$ K and $\dot{V}_{g,0} = 8$ L/min (referring to standard conditions, that is, to 0°C and 101,300 Pa), respectively. The initial molar fraction in the bulk of the liquid phase $\tilde{x}_{1,B,0}$ was either approximately 0.70 or 0.30, lying at one or the other side of the thermodynamic azeotrope. The temperature in the bulk of the gas phase $T_{g,B}$, the width of the gaps G_W, and the depth of the gaps G_D have been varied. Measured concentration curves resulting from this variation are presented in Figures 4 to 7. The data for all experiments are documented by Post.[41]

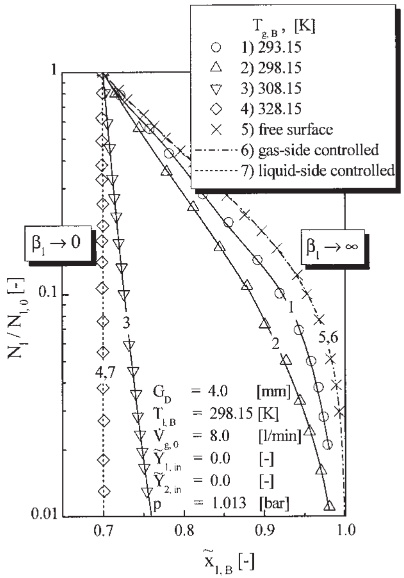

Figure 4. Concentration curves for the evaporation of a binary mixture from planar gaps into inert gas; variation of temperature in the bulk of the gas phase, $T_{g,B}$, at $\tilde{x}_{1,B,0} = 0.70$; measurements, limiting cases, and calculations (solid lines) by punctual adaptation of the liquid-side mass transfer coefficient β_l.

All the plots have two asymptotic limiting cases in common, that is, for very small and for very large liquid-side mass transfer coefficients ($\beta_l \to 0$ and $\beta_l \to \infty$, respectively). At $\beta_l \to 0$ the process is controlled by liquid-side mass transfer. Because the mixture is binary in the liquid phase, this transport step is nonselective. Consequently (see also next section), the selectivity of evaporation is zero at $\beta_l \to 0$, which corresponds to a vertical line in the plots. On the other hand, the selectivity is maximal for $\beta_l \to \infty$, determined by thermodynamic equilibrium and mass transfer in the gas. Because of the presence of air, the latter is selective in favor of water, that is, of the smaller molecule. The limiting case $\beta_l \to \infty$ can be realized experimentally by removing the porous obstacle and evaporating the well-agitated mixture from the free liquid surface. Under the already discussed conditions of dilution in the gas phase, and after the separate determination of gas-side mass transfer coefficients from pure-liquid experiments, the concentration curves can be predicted at the limit $\beta_l \to \infty$. As shown in Figures 4 and 5, the agreement of these predictions with the corresponding measurements is excellent.

With porous obstacle, but without spontaneous interfacial convection, the value of the liquid-side mass transfer coefficient would be

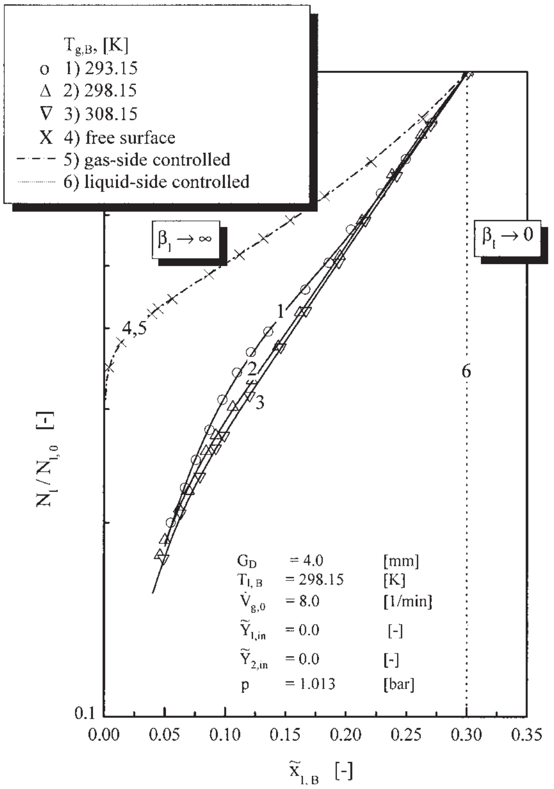

Figure 5. Concentration curves for the same conditions as in Figure 4, although at $\tilde{x}_{1,B,0} = 0.30$.

$$\beta_{l,0} = D_l/G_D \tag{3}$$

where D_l is the binary diffusion coefficient in the liquid. For every used depth of the gaps this value is so small that it may be considered to very closely represent the limiting case $\beta_l \to 0$. Consequently, all concentration curves of the Figures 4 to 7 should correspond to vertical lines without any measurable selectivity. In other words, every binary liquid of any initial concentration should behave as an azeotropic mixture. Vice versa, every deviation from the described behavior is an unequivocal proof for the existence of spontaneous, interfacial convection in the gaps. As a glance at Figures 4 to 7 reveals, such convection is the rule, not the exception. Furthermore, the extent of the deviation from the vertical line toward the opposite limit of $\beta_l \to \infty$, that is, the selectivity of the process, is a measure for the intensity of convection in the gaps.

In light of the foregoing general remarks, the phenomenology of the experimental findings can be discussed in some more detail. Starting with an initial molar fraction in the bulk of the liquid phase of $\tilde{x}_{1,B,0} = 0.70$, that means at the righthand side of the thermodynamic azeotrope, as in Figure 4, any existing selectivity can only be in favor of water. Because water is the component with the higher density and surface tension, depletion of the interface from water molecules means a decrease of density and surface tension of the interface compared to the density in the bulk of the liquid and the surface tension that liquid with the bulk molar fraction would have. This is a stable configuration with respect to both molar fraction–driven Rayleigh and molar fraction–driven Marangoni convection. Consequently, the interfacial convection evident by three of the four curves of Figure 4 can only be thermally driven, a fact additionally supported by the finding that its extent can be controlled by changing the temperature in the bulk of the gas phase, $T_{g,B}$. Indeed, the intensity of convection increases with decreasing gas bulk temperature until the limit of $\beta_l \to \infty$ is approximated. Vice versa, microconvection slows down with increasing gas bulk temperature and is not detectable at $T_{g,B} = 328.15$ K. This behavior can be explained by the fact that with decreasing gas bulk temperature the temperature of the liquid–gas interface also decreases until it becomes smaller than the temperature in the bulk of the liquid phase. Then, both density and surface tension at the interface become larger than the values corresponding to the state of the bulk liquid. As soon as some threshold is exceeded, interfacial convection is triggered and intensified by any additional decrease of the gas bulk temperature.

At the lefthand side of the azeotrope ($\tilde{x}_{1,B,0} = 0.30$; Figure 5), not only low gas bulk temperatures, but also the selective evaporation of alcohol can lead to instability, so that temperature-driven and molar fraction–driven Rayleigh and Marangoni convection may coexist. In spite of this, the measured concentration curves stay at a considerable distance from the limiting case $\beta_l \to \infty$. The influence of the gas bulk temperature is not so pronounced as in Figure 3, and the nonselective limiting case ($\beta_l \to 0$) cannot be approached. The findings indicate nonlinearities in the combination of the mentioned four possible types of interfacial convection.

Space restriction in the lateral direction inhibits the mixing influence of micro convective flow, as the results of Figure 6 from experiments with different gap widths (G_W), under otherwise the same conditions, show. For the operating conditions of Figure 6 selectivity and interfacial convection could be completely suppressed by use of the narrowest gaps with $G_W = 0.5$ mm. The same trend as in Figure 6 has been observed for every investigated gap depth.

Less clear, however, is the influence of variation of the gap depth G_D. As the data of Figure 7 show, the intensity of interfacial convection appears to increase for a gap width of $G_W = 1$ mm when increasing the gap depth (G_D) values from 1 to 4 mm, reach a maximum, and decrease again when approaching $G_D = 8$ mm. The same behavior has been found with $G_W = 1.5$ mm, but not with $G_W = 0.5$ mm. In the latter case the selectivity was observed to decrease continuously when increasing the gap depth values from 1 to 8 mm, having no detectable value at $G_D = 4$ mm (compare with Figure 6) and $G_D = 8$ mm. Penetration of the forced convective flow from the bulk of the liquid in shallow gaps cannot be the reason for the outlined behavior. Not only has such penetration been excluded by various tests (see Experimental), but it would also lead to the opposite behavior than observed in Figure 7 for a change of gap depth values from 1 to 2 mm. A satisfactory explanation for the influence of gap depth on the intensity of microconvection is still missing.

Derivation of Liquid-Side Mass Transfer Coefficients and Enhancement Factors

To quantify the findings about the influence of interfacial convection on the liquid-side mass transfer, a one-dimensional

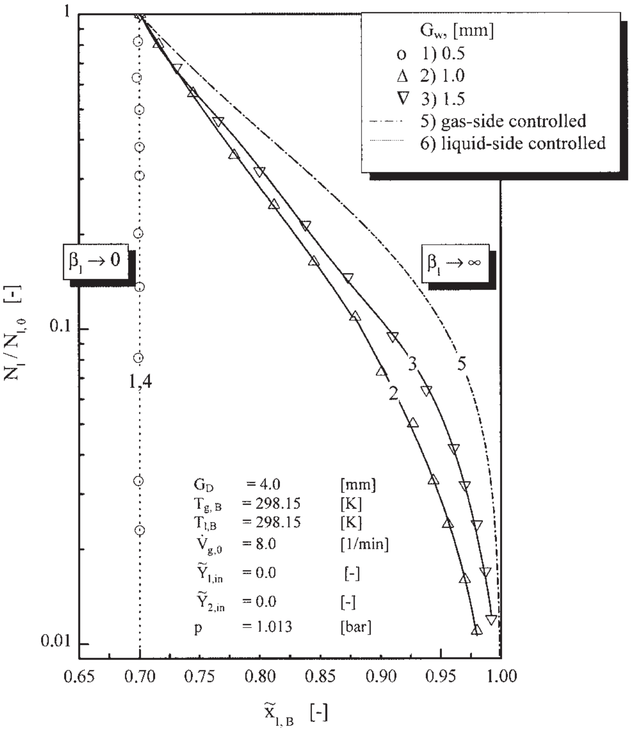

Figure 6. Concentration curves for the evaporation of a binary mixture from planar gaps into inert gas at different widths of the gaps (G_W); measurements, limiting cases, and calculations (solid lines) by punctual adaptation of the liquid-side mass transfer coefficient β_l.

model for mass and heat transfer in the gas and the liquid phase has been used. The respective mass balances for the liquid are

$$-\dot N_1 - \dot N_2 = -\dot N = \frac{dN_l}{dt} \tag{4}$$

$$-\dot N_i = \frac{d}{dt}(N_l \tilde x_{i,B}) \tag{5}$$

with $i = 1, 2$ the component index and $\dot N_i$ the molar evaporation rates. For the gas it is

$$\dot N_i = \dot N_g \tilde Y_{i,out} \tag{6}$$

with $\dot N_g$ the molar flow rate of the inert carrier (air), and $\tilde Y_{i,out}$ the molar content of vapors at the outlet of this stream ($\tilde Y_{i,in} \cong 0$).

Because of the already discussed high dilution, gas-side mass transfer kinetics may be linearized and expressed in terms of molar content; (for $\tilde y_i \ll 1$ it is: $\tilde Y_i \cong \tilde y_i$). For the ideally backmixed gas phase it, then, holds

$$\dot N_i = n_g A_{Ph} \beta_{g,i} (\tilde Y_{i,Ph} - \tilde Y_{i,out}) \tag{7}$$

Herein A_{Ph} is the gas–liquid phase contact area (cross-sectional area of the gaps). It has been pointed out that the mass transfer coefficients $\beta_{g,i}$ are determined with the help of pure-liquid evaporation experiments.

Contrary to the treatment of the gas phase, Stefan fluxes must not be neglected in the liquid, so that the relationship

$$\dot N_i = n_l A_{Ph} \beta_l \dot r_i \ln \frac{\dot r_i - \tilde x_{i,Ph}}{\dot r_i - \tilde x_{i,B}} \qquad \dot r_i = \frac{\dot N_i}{\dot N} \tag{8}$$

applies for liquid-side mass transfer kinetics. At the limit $\beta_l \to 0$, $\dot r_i - \tilde x_{i,B} = 0$ is obtained from Eq. 8. Because every component evaporates in the same proportion as it is present in the mixture ($\dot r_i = \tilde x_{i,B}$), the selectivity of the process becomes zero, and the liquid composition does not change during the process ($\tilde x_{1,B} = \tilde x_{i,B,0}$). The presence of a third species in the liquid would radically change this situation. Surplus of a component with high boiling temperature (such as glycerin) would kinetically favor the evaporation of the smaller molecule (water) in the liquid phase, in the very same way as air favors the evaporation of water in the gas phase (Eq. 7). In general, Stefan–Maxwell equations must be written for mass transfer in multicomponent liquid mixtures, and the condition of vanishing selectivity at $\beta_l \to 0$, which is typical for the binary liquid mixture, no longer applies.

At the phase boundary equilibrium according to

$$K_i = \frac{\tilde y_{i,Ph}}{\tilde x_{i,Ph}} = \frac{\gamma_i(\tilde x_{i,Ph}) p_i^0}{p} \tag{9}$$

is assumed and evaluated with the help of Antoine equations for the saturation vapor pressures, p_i^0, and the UNIQUAC method for the activity coefficients, γ_i.[41]

Notice that the above system of equations has been discussed

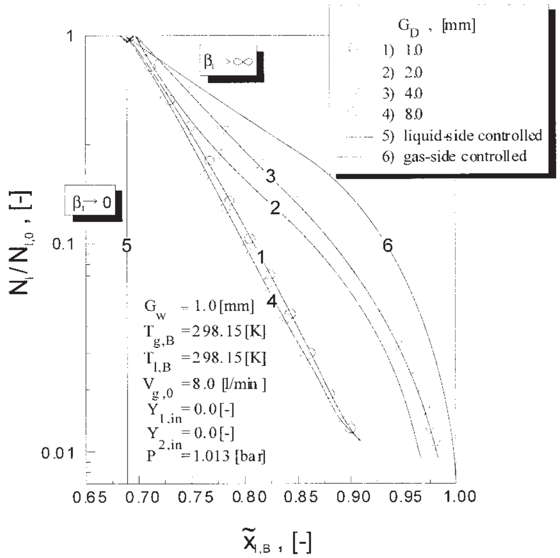

Figure 7. Concentration curves for the evaporation of a binary mixture from planar gaps into inert gas at different depths of the gaps (G_D); measurements, limiting cases, and calculations (solid lines) by punctual adaptation of the liquid-side mass transfer coefficient β_l.

in detail by previous authors,[39] including the definition and use of dimensionless separation factors for thermodynamic equilibrium, gas-side kinetics and liquid-side kinetics, limiting cases, simplified analytical solutions, and the behavior of so-called pseudoazeotropic points.

The energy balances for the gas and for the liquid boundary layer are

$$\dot{N}_g(\tilde{h}_{g,in} - \tilde{h}_{g,out}) + \sum_{i=1}^{2} \dot{N}_i \tilde{h}_{g,i}(T_{Ph}) - \dot{Q}_g = 0 \tag{10}$$

and

$$\dot{Q}_l = \sum_{i=1}^{2} \dot{N}_i[\Delta\tilde{h}_{v,i}(T_{Ph}) + \tilde{c}_{p,l,i}(T_{Ph} - T_{l,B})] - \dot{Q}_g \tag{11}$$

respectively. The heat flow rates coming from the gas ($\dot{Q}_g$) and from the liquid ($\dot{Q}_l$) are calculated by the kinetic relationships

$$\dot{Q}_g = \alpha_g K_{A,g} A_{Ph}(T_{g,B} - T_{Ph}) \tag{12}$$

$$\dot{Q}_l = \alpha_l K_{A,l} A_{Ph}(T_{l,B} - T_{Ph}) \tag{13}$$

The dimensionless quantities $K_{A,g}$ and $K_{A,l}$, so-called Ackermann corrections that account for the temperature change of the evaporation streams in the boundary layers, are for the conditions of the present investigation approximately equal to unity.[41]

The gas-side heat transfer coefficient α_g is calculated according to the Lewis analogy

$$\frac{\alpha_g}{\beta_{g,i}} = n_g \tilde{c}_{p,g} \mathrm{Le}_i^n \tag{14}$$

with

$$\mathrm{Le}_i = \frac{\lambda_g}{n_g \tilde{c}_{p,g} D_{g,i}} \tag{15}$$

from the gas-side mass transfer coefficients $\beta_{g,i}$ and the exponent n, as determined separately from pure-liquid evaporation experiments. In Eq. 15 $D_{g,i}$ are the binary diffusion coefficients of isopropanol (index: 1) and water (index: 2) in air, λ_g and $\tilde{c}_{p,g}$ are the thermal conductivity and the molar specific capacity of the gas mixture. In this context, notice that material properties referring to the phase bulks (index: B) or to the gas–liquid interface (index: Ph) are always calculated at the local values of concentration and temperature, whereas material properties referring to the boundary layers are calculated at the respective arithmetic averages.

The liquid-side heat transfer coefficient α_l has been related to the liquid-side mass transfer coefficient β_l according to

$$\alpha_l = \frac{\lambda_l \beta_l}{D_l} \tag{16}$$

which means by assuming equally thick boundary layers for temperature and concentration in the liquid and by neglecting heat transfer through the solid.

In this way, the only unknown in the system of Eqs. 4 to 16 is the liquid-side mass transfer coefficient, β_l. This is calculated by fitting the solution of the model to the experimental results for every concentration curve with measurable deviation from the limiting cases $\beta_l \to \infty$ and $\beta_l \to 0$. To this purpose, the measured concentration curve is discretized in the direction of its abscissa with a short $\Delta\tilde{x}_{1,B}$ step, and the fitting is repeated at every point, leading to a trajectory of β_l for every experiment, and to the solid lines located between the limiting cases in Figures 4 to 7. Every value of β_l derived by this method is a quantitative expression for the influence of interfacial convection on the liquid-side mass transfer. It characterizes the disturbed state of the system, is larger than the respective value of $\beta_{l,0}$ for the undisturbed state (only molecular diffusion; see Eq. 3), and may be transformed by reference to the latter to an enhancement factor

$$Eh = \frac{\beta_l}{\beta_{l,0}} \tag{17}$$

that expresses the intensification of liquid-side mass transfer by interfacial convection. By inserting Eq. 3 in Eq. 17 it is obvious that the enhancement factors could also be interpreted as liquid-side Sherwood numbers. The solution of Eqs. 4 to 16 is iterative (because of multiple coupling between the individual equations and the dependency of material properties on temperature and concentration). Brent's method (reported in Press et al.[44]) has been used for the described optimization.

Before proceeding in the next section with the discussion of enhancement factors, some characteristics of the thermal part of the model should be clarified. To this purpose, concentration curves that have been calculated with the complete model (curves 1, 2, and 3) are compared in Figure 8 with curves obtained by considering only the mass transfer (curves 4, 5, and 6). The same temperature has been assumed to prevail in the bulk of the gas and the liquid in all calculations ($T_{g,B} = T_{l,B} =$ 298.15 K). Because the liquid-side heat transfer coefficient is proportional to β_l (Eq. 16), the consideration of heat transfer has no influence at the limit $\beta_l \to \infty$; (in any case it is: $T_{Ph} = T_{g,B} = T_{l,B}$). Isothermal conditions are also valid at finite values of β_l, if heat transfer is neglected (curves 4, 5, and 6). However, by consideration of heat transfer at finite β_l, $T_{ad} < T_{Ph} < T_{l,B} = T_{g,B}$ is obtained. Because of lower interface temperatures and evaporation rates, somewhat higher selectivities are predicted when heat transfer is taken into account. The curves spread out in this range (compare curve 2 with curve 5), to fall once again together in the limiting case of $\beta_l \to 0$. Although T_{Ph} reaches its minimal value (the adiabatic, "wet-bulb" temperature T_{ad}), the direct influence of β_l dominates at $\beta_l \to 0$.

Figure 9 shows the temperature at the interface (T_{Ph}) for those calculations from Figure 8 that have been conducted with consideration of heat transfer. One interesting message of Figures 8 and 9 is that the consideration of heat transfer is not very important at relatively large values of β_l and α_l, which means for the disturbed state with considerable microconvection. In this case the difference between interface temperature T_{Ph} and liquid bulk temperature $T_{l,B}$ is relatively small (Figure 9), and

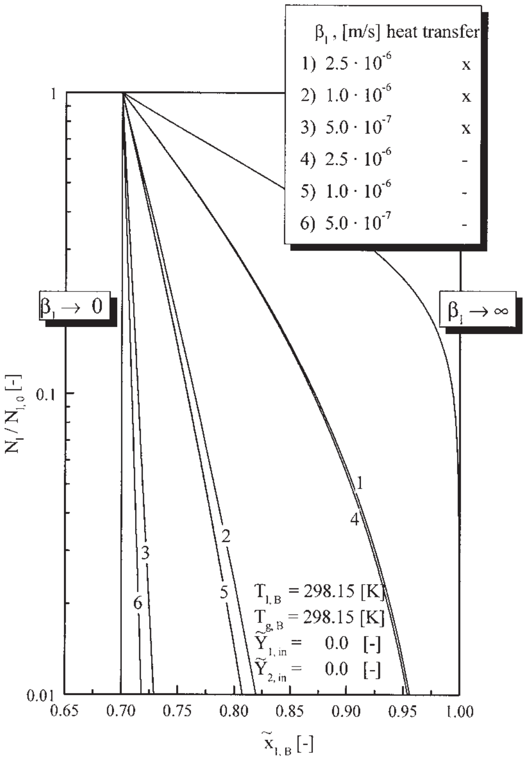

Figure 8. Concentration curves for the evaporation of isopropanol–water into air, as calculated for different liquid-side mass transfer coefficients with (×) and without (–) consideration of heat transfer from the liquid phase.

the change of selectivity arising from deviations from isothermal conditions is moderate (Figure 8). Consequently, inaccuracies in the calculation of the liquid-side heat transfer coefficient α_l according to Eq. 16 are not expected to be crucial for the described determination of enhancement factors. This situation changes, as soon as the undisturbed state of the system is considered.

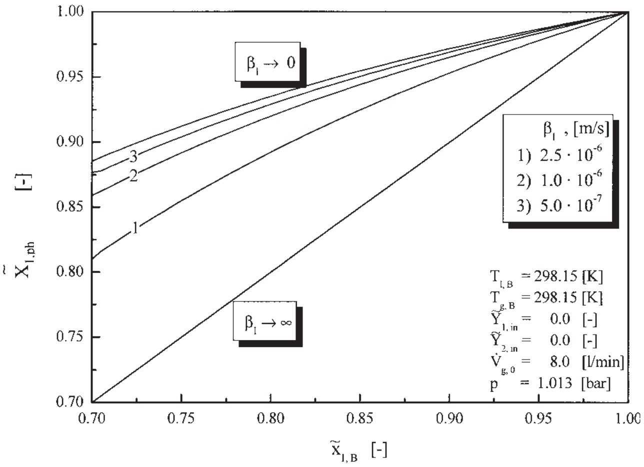

Figure 10. Interface molar fractions corresponding to the results of Figure 9.

The interface molar fractions $\tilde{x}_{1,Ph}$, resulting from the same calculations as in Figure 9, are plotted in Figure 10. Water is preferentially removed within the depicted region, so that the concentration of isopropanol is always larger at the interface than in the bulk of the liquid.

Finally, some values of the adiabatic temperature (T_{ad}) are illustrated in Figure 11 over the entire concentration range. The solid lines correspond to $\beta_l \rightarrow 0$ and $\alpha_l \rightarrow 0$, whereas the broken curves have been calculated with $\beta_l \rightarrow \infty$ and $\alpha_l \rightarrow 0$, inconsistent with Eq. 16. Given the fact that isopropanol has the higher vapor pressure, but the lower evaporation enthalpy, the adiabatic temperatures of the pure components are not very different from each other. The minimal value of T_{ad} is obtained at the pseudoazeotropic point of the system; (compare with the thermodynamic azeotrope at approximately $\tilde{x}_{l,B} = 0.66$).

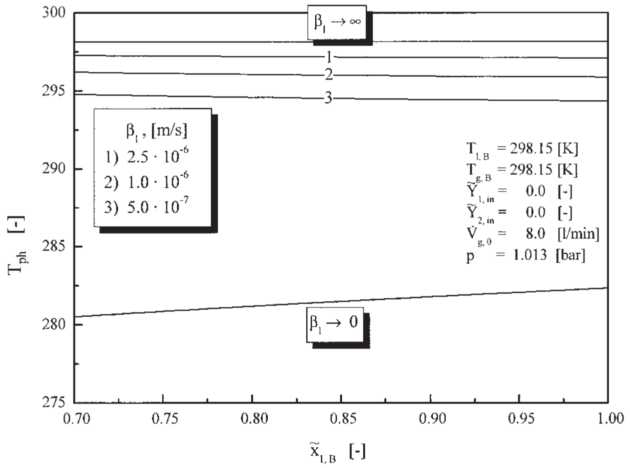

Figure 9. Interface temperatures corresponding to the calculations of Figure 8 that have been conducted with consideration of heat transfer from the liquid phase.

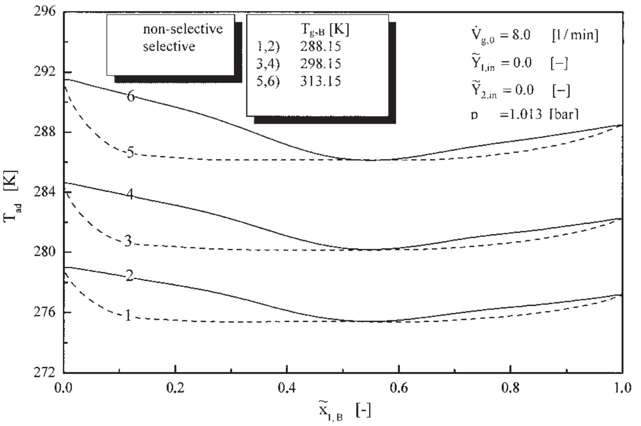

Figure 11. Adiabatic temperatures ($\alpha_l \rightarrow 0$) of the mixture isopropanol–water in air of various bulk temperatures for $\beta_l \rightarrow 0$ and $\beta_l \rightarrow \infty$.

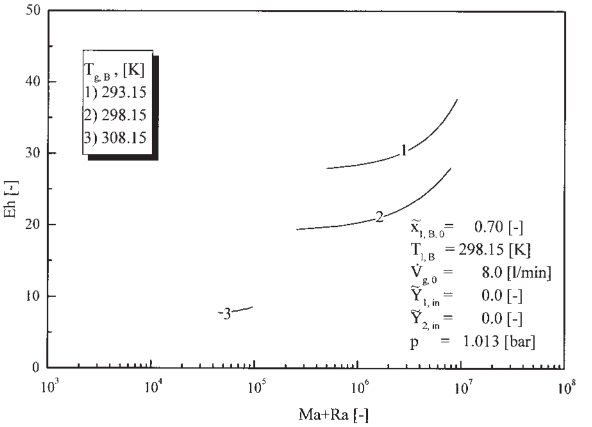

Figure 12. Enhancement factors vs. the sum of the Rayleigh and Marangoni number for the experimental data of Figure 4, that is, at different temperatures in the bulk of the gas phase for $\tilde{x}_{1,B,0} = 0.70$.

Dimensionless Driving Forces of Interfacial Convection and their Influence on Enhancement Factors

Values of β_l and Eh calculated according to the previous section express the influence of interfacial convection on liquid-side mass transfer. To also quantify the potentials giving rise to microconvection, the same model (Eqs. 4–15) has been applied to the undisturbed state of the system, which means to the state with only molecular transport mechanisms in the porous obstacle. In this case, the liquid-side mass transfer coefficient is known and equal to $\beta_{l,0}$ after Eq. 3. As already pointed out, $\beta_{l,0}$ is very small, corresponding, in terms of selectivity, to the limit $\beta_l \to 0$. Concerning the heat transfer from the liquid, combination of Eq. 3 with Eq. 16 would lead to

$$\alpha_{l,0} = \frac{\lambda_l}{G_D} \tag{18}$$

The quantity $\alpha_{l,0}$ is also very small, so that the interface temperature T_{Ph} is expected to lie in the vicinity of the adiabatic temperature T_{ad} (lowest curve in Figure 9, solid lines in Figure 11). It has been decided to conduct the calculations for the undisturbed state of the system at the limit $\alpha_l \to 0$—at not only approximately, but exactly adiabatic conditions. Under such conditions both differences $(T_{Ph} - T_{l,B})$ and $(\tilde{x}_{1,Ph} - \tilde{x}_{1,B})$ attain their maximal possible values (see Figures 9 and 10). Some critical remarks on this assumption will be given later on.

The calculation for the undisturbed state is conducted at the same points along the abscissa of the concentration curve, which means at the same values of $\tilde{x}_{1,B}$, as the previous calculation for the disturbed state. In this way, densities and surface tensions are calculated at the interface ($\rho_{l,Ph}$ resp. $\sigma_{l,Ph}$). With the differences of these values to those corresponding to the conditions of the liquid bulk (that is with $\Delta\rho_l = \rho_{l,Ph} - \rho_{l,B}$, $\Delta\sigma_l = \sigma_{l,Ph} - \sigma_{l,B}$), Rayleigh and Marangoni numbers are determined according to the definitions

$$\text{Ra} = \frac{\Delta\rho_l g G_D^3}{\eta_l D_l} \tag{19}$$

$$\text{Ma} = \frac{\Delta\sigma_l G_D}{\eta_l D_l} \tag{20}$$

and are assigned to the respective enhancement factors. This procedure enables one to interrelate driving potentials obtained from the undisturbed state of the system with enhancement factors derived from the experimental data and allocated to what is here described as the disturbed state. To control the validity of this allocation would require a rigorous, two-dimensional and dynamic treatment of transport phenomena in the porous obstacle, including momentum transport. Although such a theoretical approach may provide access to the dynamic sequences of instability development and destruction by developing interfacial convection, it is outside the scope of the present investigation.

In Eqs. 19 and 20 g is the gravity acceleration and η_l is the dynamic viscosity of the liquid. The latter, as well as the diffusion coefficient D_l, have been calculated at temperatures and concentrations corresponding to the arithmetic averages between interface and liquid bulk.

The discussed evaluation is exemplified by selected results in Figures 12 and 13. Figure 12 refers to the experimental data of Figure 4 and presents enhancement factors against the sum of the Rayleigh and the Marangoni number. In this sum only positive values of Ra and Ma are considered; negative values are set equal to zero. Such negative values would mean that the respective driving potential for interfacial convection does not exist, that is, that the configuration is stable with respect to either density or surface tension. This is indeed the case for curve 4 from Figure 4, as the separate presentation of Ra and Ma in Figure 13 reveals. The enhancement factor for this case is equal to unity, and is not plotted in Figure 12. Decreasing the gas bulk temperature to $T_{g,B} = 308.15$ K, which means going to curve 3 in Figures 4, 12, and 13, does not change the fact of negative Marangoni numbers (Figure 13). However, the Rayleigh number becomes now positive, which is accompanied by microconvection (Figure 4) with enhancement factors some-

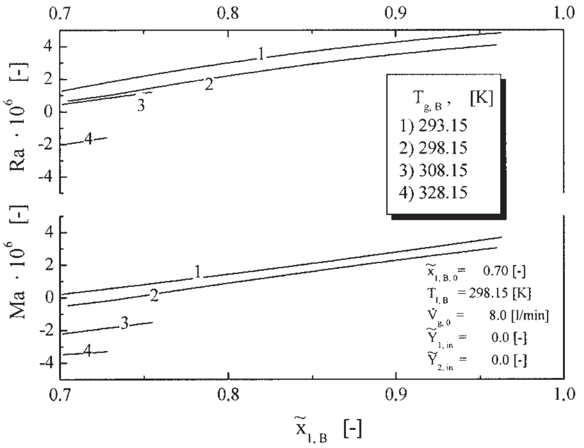

Figure 13. Separate presentation of Rayleigh and Marangoni numbers from Figure 12.

what smaller than 10 (Figure 12). Because for $\tilde{x}_{1,B,0} = 0.70$ it always is $\tilde{x}_{1,Ph} > \tilde{x}_{1,B}$ (stable situation in respect to concentration differences; compare with Figure 10), the reason for this enhancement of liquid-side mass transfer is thermally driven Rayleigh convection. This type of convection is intensified by further decrease of the gas bulk temperature, and is then accompanied by thermally driven Marangoni convection, either from the very beginning of the experiment (curve 1 in the lower part of Figure 13), or from some later point in the course of evaporation (curve 2 in the same plot). The enhancement factors increase to values between 20 and 40, far above the enhancement factors of maximally 5 that have been previously reported in literature (see Introduction).

A similar evaluation can be conducted for the data of Figures 5 to 7. It has shown enhancement factors of up to 60, regions with Ma > Ra and very large values of the sum Ra + Ma, and regions with coexisting molar fraction and temperature-driven convection. On the other hand, considerable overlap has been observed between curves in the *Eh* vs. (Ra + Ma) plots, indicating influence by additional dimensionless quantities, nonlinearities in the combination of the driving potentials, but also some influence by the consideration or not of gap width G_W and depth G_D, in the definitions of Ra, Ma, and *Eh* after Eqs. 19, 20, 17, and 3.

In a first attempt to correlate the results of the evaluation, which are all documented by Post,[41] it has been assumed that the dynamic energy created by density and surface tension differences between the interface and the bulk of the liquid is transformed to kinetic energy. Using the same length scale (the gap depth G_D) in both the density and surface tension dynamic energy terms

$$\frac{1}{2}\rho_l w^2 = g\Delta\rho_l G_D + \Delta\sigma_l/G_D \qquad (21)$$

and, after rearrangement,

$$\mathrm{Re}_{eq}^2 = 2\left(\frac{\mathrm{Ra} + \mathrm{Ma}}{\mathrm{Sc}}\right) \qquad (22)$$

is obtained with the equivalent Reynolds number

$$\mathrm{Re}_{eq} = \frac{wG_D}{\nu_l} \qquad (23)$$

and the Schmidt number

$$\mathrm{Sc} = \frac{\nu_l}{D_l} \qquad (24)$$

This is analogous to the usual derivation of simplified correlations for heat or mass transfer by combined forced and free convection, shows that the use of the sum Ra + Ma is not completely arbitrary, and introduces Sc as the additional influence parameter. On the other hand, it can only be coarsely approximate. Indeed, even in the case of conventional forced and free convection, nonlinear, supporting, or competitive combinations are well known.[45]

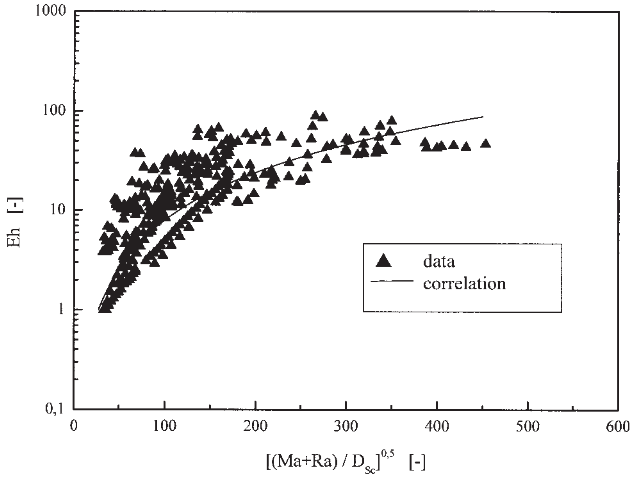

Figure 14. Measured and calculated enhancement factors for interfacial convection in planar gaps.

In the next step, the equivalent Reynolds number is considered to be proportional to the enhancement factor, the Schmidt number is replaced by a more general damping function (D_{Sc}), and factor and exponent of Eq. 22 are given free for fitting. Several trials[41] have led to the damping function

$$D_{\mathrm{Sc}} = \frac{-10538.55}{1 + \exp\left(\dfrac{x - 0.08358}{0.067567}\right)} - 10543.43 \qquad (25)$$

with

$$x = \frac{(\mathrm{Sc}_{Ph} - \mathrm{Sc}_B)_{\mathrm{disturbed}}}{(\mathrm{Sc}_{Ph} - \mathrm{Sc}_B)_{\mathrm{undisturbed}}} \qquad (26)$$

and to the correlation

$$Eh = 5 \times 10^{-3}\left(\frac{\mathrm{Ra} + \mathrm{Ma}}{D_{\mathrm{Sc}}}\right)^{4/5} \qquad (27)$$

Although the exponent of Ra or Ma is 0.5 after Eq. 22, it increases to 0.8 after fitting Eq. 27. The former is in line with the majority of existing literature; the latter is—to our knowledge—the highest value ever proposed (see Introduction). This is not necessarily unreasonable because both the enhancement factors and the dimensionless driving potentials lie in a region of high intensification of liquid-side mass transfer by interfacial convection that has never been investigated before. In fact, the exponent of the Reynolds number shows in the case of conventional forced convection a similar trend of increase with the respective argument.

The results of the correlation are compared with measured enhancement factors in Figure 14, plotted against the equivalent Reynolds number after Eq. 22 without the constant coefficient. Most points can be reproduced with deviations of less than ±100%. Although this is not too disappointing with respect to the complexity of the involved phenomena and the lack of any previous data within the investigated region, it

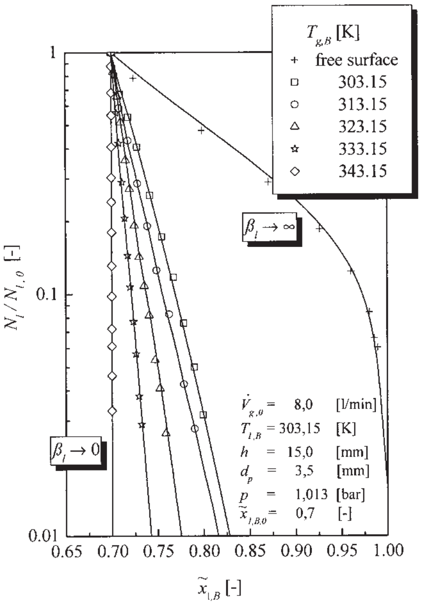

Figure 15. Concentration curves for the evaporation of a binary mixture from a packed bed into inert gas at different temperatures in the bulk of the gas phase ($T_{g,B}$) and $\tilde x_{1,B,0} = 0.70$; measurements, limiting cases, and calculations (solid lines) by punctual adaptation of the liquid-side mass transfer coefficient β_l.

certainly allows substantial room for improvement. In this context, it should be noticed that there is a fine structure in the data, which is not reflected by the correlation. Additionally, the proposed damping function requires calculations for both the disturbed and the undisturbed state (Eq. 26), is very sharp (Eq. 25), and arbitrary. That the value $Eh = 1$ is reached at finite positive values of the argument in Figure 14 is reasonable, given that the addressed problem is a stability problem. However, no comparison with the total of three experiments without measurable selectivity has yet been conducted in the sense of threshold values of the dimensionless driving forces.

Experimental Results for Evaporation from Packed Beds and their Evaluation

A total of 36 experiments have been conducted with liquid mixtures and a packed bed as the porous obstacle, varying the temperature in the bulk of the gas phase $T_{g,B}$, the particle diameter d_p, and the height of the bed h.[42] Gas flow rate, liquid bulk temperature, and initial molar fraction in the bulk of the liquid phase were the same as with sliced slabs. Measured concentration curves are presented in Figures 15 to 18 along with the limiting cases of $\beta_l \to 0$ and $\beta_l \to \infty$.

Figure 15 indicates the same influence of gas bulk temperature ($T_{g,B}$), as already observed with planar gaps. However, comparison with the corresponding plot (Figure 4) reveals a lower intensity of interfacial convection in the packed bed than in the gaps at the same gas bulk temperature. Lower permeability of the packed bed is the reason for this behavior.

At the left-hand side of the azeotrope (Figure 16, $\tilde x_{1,B,0} = 0.30$), molar fraction–driven Rayleigh and Marangoni convection is possible, arising from preferential evaporation of alcohol, and may assist the thermally initiated interfacial convection. Gas bulk temperature loses its prevailing role as the operating parameter controlling selectivity and convection. This is similar to the observations with planar gaps (compare with Figure 5). A further similarity exists in the inhibition of the mixing influence of micro convective flow by lateral space restriction. The latter has been realized in the case of packed beds by systematic decrease of the particle diameter d_p. As the data of Figure 17 show, the evaporation was nonselective for the smallest particles with $d_p = 0.23$ mm, which is equivalent to the complete absence of interfacial convection. An inhibition of the mixing influence of interfacial convection has also been observed by increasing the bed height h, as the data of Figure 18 exemplify. This trend was valid for any combination of the remaining operating and geometrical parameters. In this respect, a difference of behavior appears to exist between packed beds and planar gaps because the impact of gap depth on interfacial convection has been found to be ambiguous in the case of planar gaps (see Figure 7).

Although the further evaluation of measured data was in principle the same as that for planar gaps, some modifications have been carried out in the kinetic equations of the model, and in the definition and calculation of dimensionless numbers. These modifications will be discussed in the following.

Concerning the model, not the cross-sectional area of the gaps, but the total cross-sectional area of the space filled with the packed bed (A_0) is used in the kinetic equations for gas-side mass transfer, liquid-side mass transfer, gas-side heat transfer, and liquid-side heat transfer leading, after omission of the Ackermann factors, to

$$\dot N_i = n_g \phi A_0 \beta_{g,i}(\tilde Y_{i,Ph} - \tilde Y_{i,out}) \tag{28}$$

$$\dot N_i = n_l A_0 \beta_l \dot r_i \ln \frac{\dot r_i - \tilde x_{i,Ph}}{\dot r_i - \dot x_{i,B}} \tag{29}$$

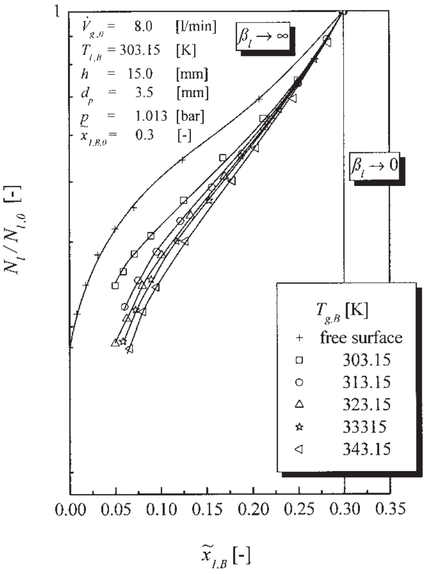

Figure 16. Concentration curves for the same conditions as in Figure 15, although at $\tilde x_{1,B,0} = 0.30$.

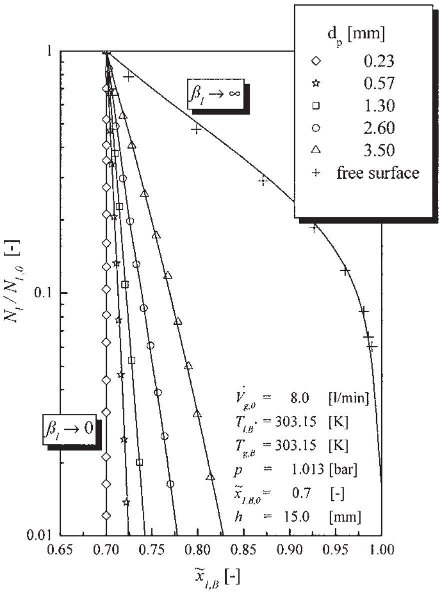

Figure 17. Concentration curves for the evaporation of a binary mixture from packed beds into inert gas at different particle diameters (d_p); measurements, limiting cases, and calculations (solid lines) by punctual adaptation of the liquid-side mass transfer coefficient β_l.

$$\dot{Q}_g = \alpha_g A_0 (T_{g,B} - T_{Ph}) \tag{30}$$

$$\dot{Q}_l = \alpha_l A_0 (T_{l,B} - T_{Ph}) \tag{31}$$

instead of Eqs. 7, 8, 12, and 13. A correction factor (ϕ) is applied to the total cross-sectional area A_0, to obtain the effective evaporation area in Eq. 28. This factor has been derived from evaporation experiments with the involved pure liquids to

$$\phi = \psi/(1 - \psi) \tag{32}$$

The same separate experiments[42] provide the gas-side mass transfer coefficients, $\beta_{g,i}$. Equations 28 and 32 define an evaporation area that is smaller than the total cross-sectional area A_0, but larger than the cross-sectional area (ψA_0) occupied by the liquid phase in the interior of the bed. This accords well with the fact that the local porosity of the packed bed increases as its free surface is approached, given that it also increases in the vicinity of rigid walls in tubular packed-bed reactors.[46]

Fitting β_l to the measured concentration curves of experiments with interfacial convection leads to the solid lines between the limiting cases of $\beta_l \to \infty$ and $\beta_l \to 0$ in Figures 15 to 18. Enhancement factors are obtained from Eq. 17. However, the liquid-side mass transfer coefficients of the undisturbed system are now set to

$$\beta_{l,0} = \frac{D_{l,bed}}{h} \tag{33}$$

with

$$D_{l,bed} = D_l(1 - \sqrt{1 - \psi}) \tag{34}$$

which means they are calculated with the effective diffusion coefficient of the bed ($D_{l,bed}$), instead of the binary liquid diffusion coefficient (D_l). Equation 34 is a well-known empirical correlation for diffusion in granular or porous media with compact and inert solids, but also for thermal, electrical, or other conduction at the limit of nonconducting particles.[47] It includes the influence of tortuosity, which is not present in the previously investigated planar gap geometry. That both tortuosity and space restriction are accounted for in the kinetic coefficient, and not explicitly in Eq. 29, is usual practice in the treatment of transport phenomena in porous media from the macroscopic perspective.

The liquid-side heat transfer coefficient α_l may, again, be assumed proportional to β_l according to the relationship

$$\alpha_l = \frac{\lambda_l \beta_l}{D_{l,bed}} \tag{35}$$

Comparison with Eq. 16 reveals that the thickness of the assumed molar fraction boundary layer is smaller for the packed beds than for the planar gaps. Because the thermal boundary layer is supposed to have the same thickness, liquid-side heat transfer coefficients after Eq. 35 are larger than those after the previous Eq. 16, indicating that the formerly neglected heat conduction through the solid phase is now—at least indirectly—accounted for. However, this is not very important for the determination of enhancement factors because for the relatively large values of β_l and α_l of the disturbed system the difference between interface temperature T_{Ph} and liquid bulk temperature $T_{l,B}$ is small (Figure 9), and the isothermal limiting case is closely approximated—more closely for the packed

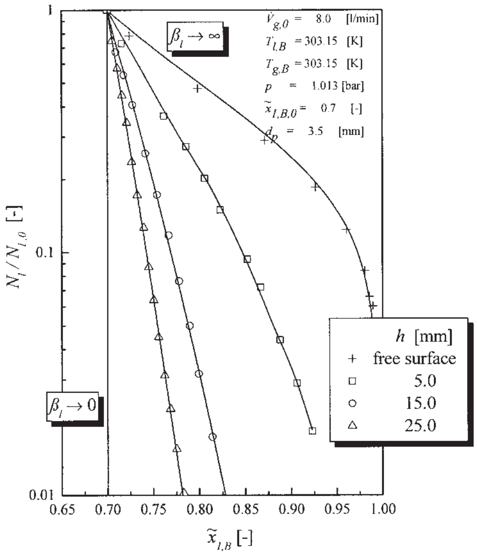

Figure 18. Concentration curves for the evaporation of a binary mixture from packed beds into inert gas at different bed heights (h); measurements, limiting cases, and calculations (solid lines) by punctual adaptation of the liquid-side mass transfer coefficient β_l.

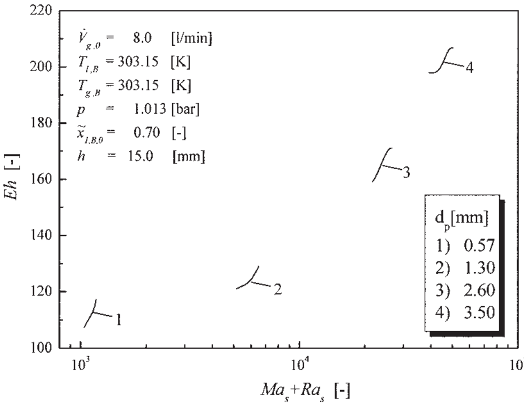

Figure 19. Enhancement factors vs. the sum of the Rayleigh and Marangoni number for the experimental data of Figure 17 (different particle diameters, d_p).

beds than for the planar gaps. Thus, the approximate character of Eq. 35 will not bias the evaluation of the disturbed state of the system.

More critical is the consideration, or not, of liquid-side heat transfer for the undisturbed state of the system. Respective calculations have been carried out at the adiabatic limit of $\alpha_l \rightarrow 0$ (as for the planar gaps), but also with heat transfer coefficients after

$$\alpha_{l,0} = \frac{\lambda_{bed}}{h} \tag{36}$$

In Eq. 36 the thermal conductivity of the quiescent bed (λ_{bed}) is calculated according to Zehner and Schlünder (see Tsotsas[47]). Equation 34 is derivable from the same model by inserting $\lambda_p = 0$, that is, by assuming nonconducting particles. However, application of Eq. 36 resulted in computing negative density and surface tension differences (stable configurations) for some experiments that were clearly accompanied by interfacial convection.[42] Such discrepancies never occurred when calculating at the adiabatic limit, so that the final evaluation for the undisturbed state of the system has been conducted at adiabatic conditions. Although this leads to a coherent interpretation of all experimental findings, the assumption of $\alpha_l \rightarrow 0$ is more questionable for packed beds than for the sliced slabs. The reason for the partial failure in the application of Eq. 36 is seen in the fact that—especially in geometrically complex media such as packed beds—local temperature differences in both axial and lateral direction may induce interfacial convection, but cannot be described with our present model, which is homogeneous and one-dimensional.

Finally, the density and surface tension differences obtained from the undisturbed-state calculations for the packed beds were transformed to so-called D'Arcy-modified Rayleigh and Marangoni numbers defined with the permeability κ, and the bed diffusion coefficient $D_{l,bed}$, as

$$\mathrm{Ra}_s = \frac{\Delta\rho_l g h \kappa}{\eta_l D_{l,bed}} \tag{37}$$

$$\mathrm{Ma}_s = \frac{\Delta\sigma_l \kappa}{\eta_l D_{l,bed} h} \tag{38}$$

The use of the permeability (Eq. 2) in these relationships enables one to account for the lateral space restriction in the porous obstacle, which is not possible with the previous Eqs. 19 and 20. In the latter, the gap depth G_D is the only length scale. The dynamic viscosity η_l and diffusivity D_l (see Eq. 34) of the liquid are calculated—as before—at the average values of temperature and molar fraction between interface and liquid bulk.

Figure 19 exemplifies the evaluation for packed beds by presenting enhancement factors derived from the experiments of Figure 17. As expected, the enhancement factor decreases with decreasing particle diameter d_p, and increases with increasing sum of Ra_s and Ma_s. Because of the consideration of the permeability of the packed beds κ, in the definition of Ra_s and Ma_s, the curves do not overlap. The separate presentation of Ra_s and Ma_s in Figure 20 indicates Rayleigh and Marangoni convection, which is thermally driven, because the initial molar fraction of the liquid lies at the right-hand side of the azeotropic point ($\tilde{x}_{1,B,0} = 0.70$). For the smallest particle diameter (d_p = 0.23 mm, lowest permeability), the evaporation is nonselective (Figure 17), and the enhancement factor is equal to unity. However—and in contrast to all nonselective experiments with planar gaps—the values of the Rayleigh and Marangoni numbers are not negative for the experiment with $d_p = 0.23$ mm. In fact, Ra_s and Ma_s have small positive values, as stated in Table 1. In this table all nonselective experiments with packed beds (5 out of 36) are summarized. In four of these experiments interfacial convection has been absent ($Eh = 1$), although Ra_s and Ma_s had positive values. This finding accords well with the stability character of the problem, and with the fact that threshold values of the driving forces must be exceeded before convective flow can take place. It also indicates that the experiments with packed beds come closer to such critical values than those with planar gaps.

With the exception of the mentioned nonselective experiment, the values of the enhancement factor range from about 110 to about 210 in Figure 19. The intensification of mass transfer is tremendous, if compared with the values of maxi-

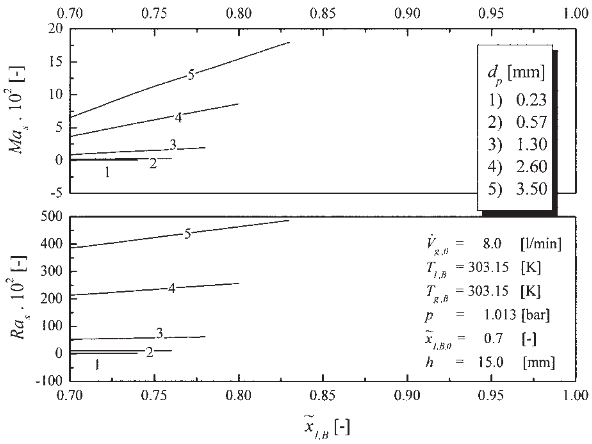

Figure 20. Separate presentation of Rayleigh and Marangoni numbers from Figure 19.

Table 1. Marangoni and Rayleigh Numbers for All Packed-Bed Experiments of the Present Investigation without Detectable Interfacial Convection (Nonselective Evaporation, $Eh = 1$)

Varied Operating Parameters							
$\tilde{x}_{1B,0}$	$T_{g,B}$ (K)	d_p (mm)	h (mm)	Ma_s	Ra_s	$\mathrm{Ma}_s + \mathrm{Ra}_s$	Eh
0.7	343.15	3.5	15.0	negative	negative	negative	1.0
0.7	303.15	0.23	5.0	8.76×10^0	5.54×10^1	6.42×10^1	1.0
0.7	303.15	0.23	15.0	2.68×10^0	1.62×10^2	1.65×10^2	1.0
0.7	303.15	0.23	25.0	1.69×10^0	2.78×10^2	2.79×10^2	1.0
0.7	303.15	0.57	25.0	1.04×10^1	1.71×10^3	1.72×10^3	1.0

mally $Eh = 5$ reported in the literature for liquid–gas systems without a porous obstacle. Compared to the evaluation for the planar gaps, the current Rayleigh and Marangoni numbers are considerably smaller. This is not a contradiction, given the different definitions of the characteristic numbers.

Analogous evaluation of concentration curves located below the azeotropic point (Figure 16) indicates that molar fraction–driven interfacial convection may be dominating in this region. The values of Ra_s and Ma_s do not change very much with the gas bulk temperature and are thus not very sensitive upon the liquid-side heat transfer coefficient. The enhancement factor increases to a remarkable value of $Eh = 2790$, the maximum obtained in the present investigation. At the same time the curves overlap in the Eh vs. ($\mathrm{Ra}_s + \mathrm{Ma}_s$) plot. A detailed discussion of the evaluation of all experimental data with packed beds is provided by Urukova,[42] including the direct comparison of β_l and $\beta_{l,0}$.

As to the correlation of the results with packed beds, Eq. 21 has been modified by using different length scales for the density and surface tension dynamic energy terms, that is, the bed height h in the former and the pore diameter d_{pore} in the latter. This is reasonable because the surface tension acts in lateral direction of the packed bed, and leads to the expression

$$\frac{1}{2}\rho_l w^2 = g\Delta\rho_l h + \Delta\sigma_l/d_{pore} \tag{39}$$

The average pore diameter of the packed bed may be calculated to

$$d_{pore} = \frac{2}{3}\frac{\psi}{1-\psi}d_p \tag{40}$$

After rearrangement, and for an average bed porosity of $\psi = 0.36$,

$$\mathrm{Re}_{eq}^2 = 166.67\left(\frac{\mathrm{Ra}_s + \Gamma\,\mathrm{Ma}_s}{\mathrm{Sc}}\right) \tag{41}$$

is obtained, with

$$\Gamma = \frac{3(1-\psi)h}{2\psi d_p} \tag{42}$$

the equivalent Reynolds number

$$\mathrm{Re}_{eq} = \frac{ud_p}{(1-\psi)\nu_l} \tag{43}$$

and the superficial velocity

$$u = w/\psi \tag{44}$$

In the next step, the equivalent Reynolds number is considered to be proportional to the enhancement factor, and the factor and exponent of Eq. 41 are fitted, yielding

$$Eh = 29.47\left(\frac{\mathrm{Ra}_s + \Gamma\,\mathrm{Ma}_s}{\mathrm{Sc}}\right)^{4/5} \tag{45}$$

The results of this correlation are compared with measured enhancement factors in Figure 21, plotted against the equivalent Reynolds number after Eq. 41 without the constant coefficient. With respect to the attempt of correlating the data for planar gaps (Figure 14), the performance of Eq. 45 is not better. However, Eq. 45 contains just the Schmidt number, which is calculated as the arithmetic average of the Schmidt numbers corresponding to the interface and liquid bulk conditions for the disturbed state of the system. Contrarily, an argument combining interface and bulk values of the Schmidt number for the disturbed and the undisturbed system has been used previously (Eq. 26), combined with a sharp, complex, and arbitrary damping function (Eq. 25). The fact that such a damping

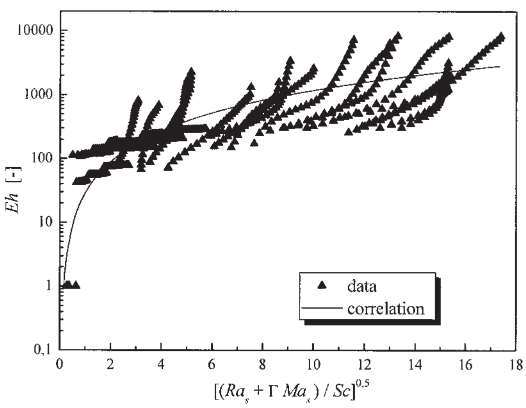

Figure 21. Measured and calculated enhancement factors for interfacial convection in packed beds.

function is not introduced in Eq. 45 is considered to be a clear advantage.

As to the exponent of the Rayleigh or Marangoni number, it has with 0.8 the same value for the packed beds and for the planar gaps. It has been pointed out before that this is larger than any previously reported value, which is explained by the fact that our experiments were conducted in a region of exceptionally high intensification of liquid-side mass transfer. The results of the investigation with packed beds appear to support this argumentation. It should also be noticed that an asymmetry between the Rayleigh and the Marangoni number is introduced in Eq. 41, depending on structural parameters of the porous medium (Eq. 42). This type of asymmetry has scarcely been discussed before and may deserve closer consideration in future work. In general, significant opportunities of improvement remain with respect to the overall predictive performance of the correlation, the obvious and not properly described fine structure of the data (Figure 21), the consideration of critical values of the dimensionless driving potentials, and the extrapolation to systems without a porous obstacle.

Conclusions and Outlook

A new experimental method for investigating the influence of interfacial convection on liquid-side mass transfer has been introduced. The method consists of evaporating a binary liquid mixture (water and isopropanol) from a porous obstacle into inert gas (air) and measuring the change of liquid bulk molar fraction with changing amount of liquid (concentration curve). Because of the large diffusive resistance of the liquid-filled porous obstacle, nonselective evaporation is expected for the "undisturbed state" of the investigated system. Such nonselective evaporation could be established at specific experimental conditions, but is rather unusual. Usually, selective concentration curves are measured, which proves the existence of spontaneous interfacial convection in the porous obstacle. By application of a one dimensional model for mass and heat transfer, liquid-side mass transfer coefficients can be derived from every selective concentration curve, quantifying the enhancement of liquid-side mass transfer by interfacial phenomena in the "disturbed state" of the system. The same evaluation without convection yields differences of density and/or surface tension between the interface and the liquid bulk, which can be transformed to dimensionless driving potentials in form of Rayleigh and Marangoni numbers.

To reliably and reproducibly conduct the described experiments, two different measuring devices have been designed and applied. In the first one, the porous obstacle was a rectangular plate with parallel, planar gaps. In the second, cylindrical packed beds of equally sized spherical particles constituted the obstacle. The experiments have been conducted for various gas bulk temperatures, and for initial liquid bulk molar fractions at either side of the thermodynamic azeotrope of the mixture. Additionally, width and depth of the gaps, particle diameter, and bed height have been varied.

In this way, it could be shown how the intensity of interfacial convection can be deliberately controlled by even small changes of the bulk temperature of the gas phase. Thermally driven Rayleigh and Marangoni convection combine at initial liquid molar fractions above the azeotropic point, whereas they typically coexist with molar fraction driven Rayleigh and Marangoni convection below the azeotrope. Convection is inhibited by lateral space restriction and was thus found to decrease with decreasing gap width or particle diameter.

Derived enhancement factors are much larger than previously reported in the literature (up to almost 100 for the sliced slabs and to almost 2800 for the packed beds, compared to previously documented values of maximally about five). Although our presented correlation attempts are still coarse and preliminary, they do indicate a strong dependency of the enhancement factor on the Rayleigh or Marangoni number, with an exponent of 0.8 instead of, typically, 0.5 in the literature. This is explained by the fact that the experiments were conducted in a region of high intensification of liquid-side mass transfer that had never been previously investigated.

The appropriate consideration of structure and permeability of the porous medium has been discussed, along with the definition of D'Arcy-modified Rayleigh and Marangoni numbers for the packed beds. It has been pointed out that the present evaluation is, with respect to liquid-side heat transfer, close to the isothermal limit for the disturbed and adiabatic for the undisturbed state of the system. Although the former is reasonable and not very important for the result of the evaluation, the latter may be problematic; however, this is hardly avoidable in the frame of a simplified one-dimensional model. Finally, four nonselective experiments with packed beds have been identified, which correspond to small, but positive values of the dimensionless driving potentials, underlining the stability character of the problem under consideration.

One obvious continuation of the present work would be to systematically identify critical Rayleigh and Marangoni numbers by use of such methods as smaller increments in the variation of gas bulk temperature above the azeotropic point. Such experiments must be combined with a rigorous stability analysis and—in the perspective—with a more fundamental, two-dimensional modeling of transport phenomena in the porous obstacle. On the other hand, the developed experimental method allows for a systematic variation of liquid properties, either by additives or by use of alternative binary mixtures. In this way, a better understanding of the underlying, complex phenomena may be achieved, along with better, more accurate correlations.

In total, the presented method may be seen as *complementary* to previous experimental approaches referring closely to processes such as liquid–liquid extraction, absorption or distillation—complementary in the sense of enabling the investigation of otherwise inaccessible regions of high enhancement of liquid-side mass transfer. Consequently, and by extrapolation, it may contribute to a better understanding of the influence of interfacial phenomena on such processes. However, the used porous obstacles are not of interest only as artificial models for thick laminar boundary layers, but also for their own sake as membranes, catalysts, products to be dried, and soils in numerous chemical and environmental engineering applications.

Acknowledgments

The described research was supported in part by the postgraduate program of the German federal state of Saxony–Anhalt and by the Max-Buchner-Foundation.

Notation

A_{ph} = gas–liquid phase contact area, m^2

A_0 = total cross-sectional area, m^2
$\tilde{c}_p$ = molar heat capacity, J mol^{-1} K^{-1}
d = diameter, m
D = diffusion coefficient, m^2/s
D_{Sc} = damping function
Eh = enhancement factor
g = acceleration of gravity, m/s^2
G = gap dimension, m
h = height, m
$\tilde{h}$ = molar enthalpy, J/mol
$\Delta\tilde{h}_v$ = molar evaporation enthalpy, J/mol
K = equilibrium coefficient
K_{A} = Ackermann correction factor
Le = Lewis number, Eq. 15
n = molar density, mol/m^3
N = molar amount, mol
$\dot{N}$ = molar flow rate, mol/s
Ma = Marangoni number, Eq. 20
Ma$_s$ = D'Arcy-modified Marangoni number, Eq. 38
p = pressure, Pa
$\dot{Q}$ = heat flow rate, W
$\dot{r}$ = relative molar evaporation flux
Ra = Rayleigh number, Eq. 19
Ra$_s$ = D'Arcy-modified Rayleigh number, Eq. 37
Re$_{\mathrm{eq}}$ = equivalent Reynolds number, Eqs. 23 and 43
Sc = Schmidt number, Eq. 24
t = time, s
T = temperature, K or °C
u = superficial velocity, m/s
$\dot{V}$ = volume flow rate, m^3/s
w = flow velocity, m/s
x = parameter of damping function
$\tilde{x}$ = liquid molar fraction
$\tilde{y}$ = gas molar fraction
$\tilde{Y}$ = molar content, mol$_{\mathrm{vapor}}$/mol$_{\mathrm{inert\ gas}}$

Greek letters

α = heat transfer coefficient, W m^{-2} K^{-1}
β = mass transfer coefficient, m/s
γ = activity coefficient
Γ = structural coefficient, Eq. 42
η = dynamic viscosity, kg m^{-1} s^{-1}
κ = permeability, m^2
λ = thermal conductivity, W m^{-1} K^{-1}
ν = kinematic viscosity, m^2/s
ρ = density, kg/m^3
σ = surface tension, kg/s^2
ϕ = correction factor, Eq. 32
ψ = porosity

Indices

ad = adiabatic
bed = bed
B = bulk
D = depth
g = gas
i = species (1: isopropanol, 2: water)
in = inlet
l = liquid
out = outlet
p = particle
pore = pore
Ph = interface
W = width
0 = initial
0 = saturation
0 = undisturbed (stable) state
0 = standard conditions

Literature Cited

1. Kazhdan D, Shtilman L, Golovin AA, Prismen LM. Non-linear waves and turbulence in Marangoni convection. *Phys Fluids.* 1995;7:2679-2685.
2. Severin J, Herwig H. Onset of convection in the Rayleigh–Bénard flow with temperature dependent viscosity: An asymptotic approach. *Z Angew Math Phys.* 1999;50:375-386.
3. Bragard J, Velarde MG. Bénard–Marangoni convection: Plan forms and related theoretical predictions. *J Fluid Mech.* 1998;368:165-194.
4. Birikh RV, Briskman VA, Rudakov RN, Velarde MG. Marangoni–Bénard instability of a floating liquid layer with an internal, permeable, heated or cooled divider and two deformable, open surfaces. *Int J Heat Mass Transfer.* 1995;38:2723-2731.
5. Or AC, Kelly RE. Onset of Marangoni convection in a layer of fluid modulated by a weak nonplanar oscillatory shear. *Int J Heat Mass Transfer.* 1995;38:2269-2279.
6. Golovin AA, Nepomnyashchy AA, Pismen LM, Riecke H. Steady and oscillatory side-band instabilities in Marangoni convection with deformable interface. *Physica D.* 1997;106:131-147.
7. Hashim I, Wilson SK. The onset of oscillatory Marangoni convection in a semi-infinitely deep layer of liquid. *Z Angew Math Phys.* 1999;50:546-558.
8. Boeck T, Thess A. Bénard–Marangoni convection at low Prandtl number. *J Fluid Mech.* 1999;399:251-275.
9. Li M, Zheng D, Zhu T. Instability of the Marangoni convection in a liquid bridge with liquid encapsulation under microgravity condition. *Int J Heat Mass Transfer.* 2002;45:157-164.
10. Tan KK, Thorpe RB. The onset of convection driven by buoyancy effects caused by various modes of transient heat conduction: Part I. Transient Rayleigh numbers; Part II. The sizes of plumes. *Chem Eng Sci.* 1999;54:225-238,239-244.
11. Gottberg von FK, Hatton TA, Smith KA. Surface instabilities due to interfacial chemical reaction. *Ind Eng Chem Res.* 1995;34:3368-3379.
12. Mendes-Tatsis MA, Pérez de Ortiz ES. Marangoni instabilities in systems with an interfacial chemical reaction. *Chem Eng Sci.* 1996;51:3755-3761.
13. Kang KH, Choi CK, Hwang IG. Onset of solutal Marangoni convection in a suddenly desorbing liquid layer. *AIChE J.* 2000;46:15-23.
14. Skarda JRL, McCaughan FE. Exact solution to stationary onset of convection due to surface tension variation in a multicomponent fluid layer with interfacial deformation. *Int J Heat Mass Transfer.* 1999;42:2387-2398.
15. Bau HH. Control of Marangoni–Bénard convection. *Int J Heat Mass Transfer.* 1999;42:1327-1341.
16. Sternling CV, Scriven LE. Interfacial turbulence: Hydrodynamic instability and the Marangoni effect. *AIChE J.* 1959;5:514-523.
17. Pérez de Ortiz ES, Sawistowski H. Interfacial stability of binary liquid–liquid systems, Part I: Stability analysis. *Chem Eng Sci.* 1973;28:2051-2062.
18. Imaishi N, Fujinawa K. Theoretical study of the stability of two-fluid layers. *J Chem Eng Jpn.* 1974;7:81-86.
19. Reichenbach J, Linde H. Linear perturbation analysis of surface-tension-driven convection at a plane interface (Marangoni instability). *J Colloid Interface Sci.* 1981;84:433-438.
20. Wassmuth F, Laidlaw WG, Coombe DA. Interfacial instabilities: The Linde instability. *Chem Eng Sci.* 1990;45:3483-3490.
21. Wolf S. *Phasengrenzkonvektionen beim Stoffübergang in Flüssig-Flüssig-Systemen* (PhD Thesis, Technical Univ. of Munich). Fortschritt-Berichte VDI, Series 3, No. 584. Düsseldorf, Germany: VDI-Verlag; 1999.
22. Chai AT, Zhang N. Experimental study of Marangoni–Bénard convection in a liquid layer induced by evaporation. *Exp Heat Transfer.* 1998;11:187-205.
23. Guzun-Stoica A, Kurzeluk M, Floarea O. Experimental study of Marangoni effect in a liquid–liquid system. *Chem Eng Sci.* 2000;55:3813-3816.
24. Pertler M, Häberl M, Rommel W, Blaβ E. Mass-transfer across liquid-phase boundaries. *Chem Eng Process.* 1995;34:269-277.
25. Henschke M, Pfennig A. Mass-transfer enhancement in single-drop extraction experiments. *AIChE J.* 1999;45:2079-2086.
26. Semkov K, Kolev N. On the evaluation of the interfacial turbulence (the Marangoni effect) in gas (vapour)–liquid mass transfer: Part I. A method for estimating the interfacial turbulence effect; Part II. Mod-

elling of packed columns accounting for axial mixing and Marangoni effects. *Chem Eng Process*. 1991;29:77-82,83-91.
27. Proctor SJ, Biddulph MW, Krishnamurthy KR. Effects of Marangoni surface tension forces on modern distillation packings. *AIChE J.* 1998;44:831-835.
28. Wu H, Chung TW, Lai MH. Effects of Marangoni convection on the mass transfer performance in a packed-bed absorber. *Ind Eng Chem Res.* 2001;40:885-891.
29. Vazquez G, Antorrena G, Navaza JM, Santos V. Absorption of CO_2 by water and surfactant solutions in the presence of induced Marangoni effect. *Chem Eng Sci.* 1996;51:3317-3324.
30. Lu HH, Yang YM, Maa JR. Effect of artificially provoked Marangoni convection at a gas/liquid interface on absorption. *Ind Eng Chem Res.* 1996;35:1921-1928.
31. Lu HH, Yang YM, Maa JR. Surfactant effects on absorption in the presence of induced interfacial turbulence. *AIChE J.* 1997;43:1909-1913.
32. Smigelschi O, Suciu DG, Ruckenstein E. Absorption under the action of artificially provoked Marangoni effect. *Chem Eng Sci.* 1969;24: 1227-1234.
33. Ruckenstein E, Berbente C. The effect of roll-cells on mass transfer. *Chem Eng Sci.* 1970;9:475-482.
34. Linde H, Schwarz P. Prinzipien der Grenzflächendynamik—Ein neues Berechnungsmodell für den konvektiven Stoff- und Wärmeübergang über fluide Grenzen unter Berücksichtigung des Schubspannungsgleichgewichtes. *Chem Technol.* 1974;26:455-457.
35. Ostrovskii MV, Barsukov II, Abramzon AA. The effect of spontaneous surface convection on mass-transfer coefficient. *Int Chem Eng.* 1974;14:431-438.
36. Imaishi N, Suzuki Y, Hozawa M, Fujinawa K. Interfacial turbulence in gas–liquid mass transfer. *Int Chem Eng.* 1982;22:659-665.
37. Pikkov LM, Rabinovich LM. Calculating rate of mass transfer in a liquid in the presence of the Marangoni effect. *Theor Fundam Chem Eng.* 1989;23:104-108.
38. Sun ZF, Yu KT, Wang, SY, Miao YE. Absorption and desorption of carbon dioxide into and from organic solvents: Effects of Rayleigh and Marangoni instability. *Ind Eng Chem Res*. 2002;41:1905-1913.
39. Riede T, Schlünder EU. Selective evaporation of a binary mixture into dry or humidified air. *Chem Eng Process.* 1990;27:83-93.
40. Schwarzbach J, Nilles M, Schlünder EU. Microconvection in porous media during pervaporation of a liquid mixture—An experimental study. *Chem Eng Process.* 1987;22:163-175.
41. Post S. *Zum Einfluβ von Grenzflächenkonvektionen auf die Stoffübertragung am Beispiel der selektiven Verdunstung eines binären Gemisches aus ebenen Spalten* (PhD Thesis, Univ. of Magdeburg). Fortschritt-Berichte VDI, Series 3, No. 722. Düsseldorf, Germany: VDI-Verlag; 2002.
42. Urukova I. Einfluβ der Mikrokonvektion auf Selektivität und Stofftransport während der Verdunstung binärer Flüssigkeiten aus porösen Schichten. PhD Thesis. Magdeburg, Germany: Univ. of Magdeburg; 2005.
43. Henneberg M, Ziad Saghir M, Rednikov A, Legros JL. Porous media and the Bénard–Marangoni problem. *Transport Porous Media.* 1997; 27:327-355.
44. Press WH, Flannery BP, Teukolsky SA, Vetterling WT. *Numerical Recipes*. Cambridge, UK: Cambridge Univ. Press; 1989.
45. Klan H. *Wärmeübergang durch Mischkonvektion an umströmten Körpern*. VDI-Wärmeatlas, Section Fe. 9th Edition. Berlin: Springer-Verlag; 2002.
46. Winterberg M, Tsotsas E, Krischke A, Vortmeyer D. A simple and coherent set of coefficients for modelling of heat and mass transport with and without chemical reaction in tubes filled with spheres. *Chem Eng Sci.* 2000;55:967-979.
47. Tsotsas E. Heat transfer to gas–solid systems: Stagnant packed beds. *Heat Exchangers Design Update*. Section 2.8.1. New York, NY: Begell House; 2000.

Manuscript received May 11, 2004, and revision received Mar. 18, 2005.